Journal of Power Sources 189 (2009) 1051–1059

Contents lists available at ScienceDirect

Journal of Power Sources

journal homepage: www.elsevier.com/locate/jpowsour

Computation of TPB length, surface area and pore size from numerical reconstruction of composite solid oxide fuel cell electrodes

Ben Kenney[a,b], Mikelis Valdmanis[a,c], Craig Baker[a,c], J.G. Pharoah[a,c,*], Kunal Karan[a,b]

[a] Queen's-RMC Fuel Cell Research Centre, Queen's University, Kingston, ON, Canada
[b] Department of Chemical Engineering, Queen's University, Canada
[c] Department of Mechanical and Materials Engineering, Queen's University, Canada

ARTICLE INFO

Article history:
Received 13 November 2008
Received in revised form
23 December 2008
Accepted 24 December 2008
Available online 17 January 2009

Keywords:
SOFC
Electrode
Composite
Optimization
Reconstruction
Microstructure

ABSTRACT

A numerical technique for generating the solid oxide fuel cell composite electrode structure based on measurable starting parameters has been developed. This method can be used to calculate all relevant electrode microstructural parameters. The structures are formed of randomly distributed overlapping spheres with particle size distributions that match the particle sizes of actual ceramic powders. In this work, the triple phase boundary length, internal surface area, pore size and the percolation of all relevant phases within the porous composite electrode were computed. It was found that the triple phase boundary length computed for particles with real particle size distributions was as much as 40% lower compared to mono-sized particles with the same mean particle sizes. Percolation thresholds were in the range of 30–40 vol% for solid phases and over 99% of pores were found to belong to a percolating network at porosities as low as 25%. In addition, the average pore size was found to be 0.19 μm for typical electrode compositions, smaller than what is commonly assumed and in certain circumstances, the distribution of pore sizes may place gas transport in the free molecular flow regime.

1. Introduction

The overall process of electro-reduction of an oxidant or electro-oxidation of a fuel in a fuel cell electrode comprises several elementary reaction and transport steps. For typical solid oxide fuel cell (SOFC) cathodes, these can include gas-phase transport of oxygen, adsorption onto the electro-catalyst surface, surface diffusion of adsorbed oxygen species, electron conduction through the electro-catalyst phase, ion conduction through the ion-conducting phase and the charge-transfer reaction. The charge-transfer step is considered to occur at sites where the reaction constituents – electrons, ions and chemical species (oxygen) – can simultaneously co-exist. Such sites are called triple-phase boundaries (TPBs), i.e. the boundary where the three distinct phases transporting the three distinct reactants meet. The composite nature of the SOFC cathode – mixture of LSM electro-catalyst and ion-conductor YSZ – afford a large number of triple phase boundaries within the porous structure. However, only those TPBs can be active for which each of the three phases belong to a percolating network so as to allow transport of the relevant reactant species. For enhanced electrochemical performance, it is generally desirable to increase the number of TPBs although maximization of overall electrochemical performance requires consideration of transport effects, in particular the ionic conduction [1].

For SOFC cathodes, the overall rate of oxygen reduction will be dependent on the rates of the individual steps. The rates of the chemical/physical steps are proportional to the characteristic dimension for the kinetic and transport processes. For example, the rate of bulk transport of any one of the three reacting species – oxygen, ion, and electron – is dependent on the length of the tortuous path while the rate of adsorption is proportional to the gas–solid internal surface area and the rate of the charge transfer reaction is proportional to the TPB length (TPBL). For porous composite structures, the characteristic microstructural dimensions are a function of the primary particle size and distribution of the three phases. The particle sizes of LSM and YSZ and the type of pore formers employed affects the TPBL and LSM-pore interface area and thereby the electrode performance. For example, Ostergard et al. [2] showed that, for $La_{0.85}Sr_{0.15}MnO_3$ cathodes, tailoring the morphology of the powder could decrease the electrode resistance by over seven times. They also reported an additional fivefold performance increase by creating a composite electrode. These performance increases were attributed to improved contact with the bulk electrolyte as well as an extended TPBL in the composite structure. Although, this study showed empirically that improvement in performance was

* Corresponding author at: Queen's-RMC Fuel Cell Research Centre, Queen's University, McLaughlin Hall, Kingston, ON, Canada K7L 3N6. Tel.: +1 613 533 6579; fax: +1 613 533 6489.
E-mail address: pharoah@me.queensu.ca (J.G. Pharoah).

0378-7753/$ – see front matter © 2009 Elsevier B.V. All rights reserved.
doi:10.1016/j.jpowsour.2008.12.145

achieved through enhanced TPBL, a quantitative correlation was not presented.

Quantification of active TPBL and other microstructural parameters such as electro-catalyst surface area and porosity of porous composite are essential for comparing the performance of two different electrodes but, more importantly, for the determination of optimum structure/composition that yields maximum electrochemical performance. Experimental determination of total internal surface area, porosity and pore size are possible. For example, in principle, the total internal surface area, the porosity and/or pore size distribution can be obtained via the liquid nitrogen (or krypton) BET adsorption measurements and mercury intrusion porosimetry. However, in practice, these instruments must be extremely sensitive in order to measure the low surface areas and pore volumes of the electrodes. Moreover, the measured internal surface area does not distinguish between the surface area of the two different solid materials (LSM and YSZ in case of SOFC composite cathode) and pore size measurements are highly dependent on the technique being used. Quantitative stereological methods have been used to estimate the internal surface area from 2D images [3,4] but relies on the resolution of the image, making analysis of small features difficult.

Experimental methods for determination of TPBL of composite electrodes again rely primarily on stereological methods [3]. Recent attempts to reconstruct porous electrodes from FIB-SEM images [5] offer promise but the resolution of the SEM images (in the order of 50–100 nm) and phase identification pose some challenge. Theoretical approach for estimation of TPBL has been based on coordination particle theory that allows calculation of the percolation and coordination number of binary random packed spheres [6–8,1,9]. This approach is limited to mono-sized particles and by the fact that the particle–particle contact angle is not coupled to the electrode porosity. More recently, Schneider et al. [10] as well as Golbert et al. [11] reconstructed the approximate electrode geometry to avoid volume average modelling techniques altogether. Martinez and Brouwer [12] as well as Ali et al. [13] have also developed geometrical models to evaluate the TPBL in composite electrodes. In the case of Ali et al., their analysis concluded that the spatial distribution of active reaction sites could be important and that layers such as a current collector layer can increase the overall TPBL. The works by Schneider et al., Golbert et al., Martinez and Brouwer and Ali et al. have so far used mono-sized particles, however, ceramic powders can have broad particle size distributions which can have a large impact on the microstructure. In addition, the previous work mainly focused on calculation of the triple phase boundary and did not report other microstructural parameters such as the internal surface area and the pore size distribution. Both of these parameters may be important under certain circumstances such as slow adsorption kinetics or if the pore sizes are small enough to restrict gas transport to the free molecular flow regime.

In this work, we present a technique that can be used to determine all relevant microstructural parameters as well as effective transport properties, by numerically generating the composite electrode structure based on measurable parameters of the starting ceramic powder and subsequent numerical analysis to determine the relevant parameters. The focus of the present work is the determination of the triple phase boundary length, LSM–YSZ contact area, internal surface area and the pore size distribution as a function of particle size, composition of solid matrix constituents (LSM and YSZ) and overall porosity.

2. Method

In the following we describe the algorithm for structure generation as well as calculation of the triple phase boundary length, particle contact area, internal surface area, pore percolation and pore size distribution. This was developed using the C programming language.

Although the method and results presented here are general and can be applied to both composite anodes and cathodes, for this work, we have denoted one particle type as LSM and the other as YSZ to represent a composite cathode. The input parameters for the structure included the LSM and YSZ particle size distributions, overall porosity and the solid volume fraction for each particle type.

2.1. Structure generation

All particles were considered to be spherical and the porous structures were formed of randomly distributed particles. Particle size distributions in this work were implemented by assuming a normal distribution, however, any type of distribution could be implemented. The algorithm consisted of randomly dropping a particle into a domain of specified dimensions. The particle was allowed to roll over other particles until it either touched three other particles or the bottom of the domain, at which point its position was fixed. The desired solid volume fraction of the LSM and YSZ phases were enforced by assigning a weighted probability to the particle selection before the particle was dropped. The domain boundary conditions in the horizontal directions were periodic.

During their fabrication, SOFC electrodes undergo sintering of particles. To capture this effect, the minimum allowable distance between two contacting particles was varied until the desired structure porosity was obtained. Essentially this varied the particle–particle contact angle allowing for densification of the structure, simulating various degrees of sintering. This contact angle was a function of the size ratio of the contacting particles and is not constant throughout the structure.

Using this structure generation technique, the centre coordinate, the particle size and the contacting particles were known for each particle within the domain. We were able to determine whether each particle in the structure belonged to a percolating network by tracking the connecting neighbors of each particle. It was assumed that LSM particles in the first layer belonged to a percolating network and that YSZ particles in the last layer also belonged to a percolating network. This was equivalent to placing a current collector on the top layer and having the bulk electrolyte along the bottom layer.

2.2. Triple phase boundary length, contact area and internal surface area calculation

For each structure, the total and active triple phase boundary lengths were calculated. The active TPBs were calculated using only those particles that belonged to a percolating network. The calculation was done using two different techniques: (1) an analytical technique and (2) a grid based counting technique. The analytical technique calculated the TPBs directly with the knowledge of the geometry of each contacting LSM and YSZ pair, as shown in Fig. 1(a) and Eqs. (1)–(3). This is possible since the centre-point coordinates (x, y, z) and sizes of each particle were known. For the simple case of a single LSM particle contacting a single YSZ particle, the distance between the two centre point locations and the particle radii were used to calculate the circumference of the outer edge of the contact circle as well as the contact area. In a similar manner, the internal surface area was calculated by calculating the surface area of each sphere and subtracting the surface area that was inaccessible due to particle overlap. For this method, special attention was given to account for a third particle intersecting part of the contact circle between an LSM–YSZ pair or a third particle contributing to the surface area calculation. This situation was primarily encountered at low porosities. To account for the volume and

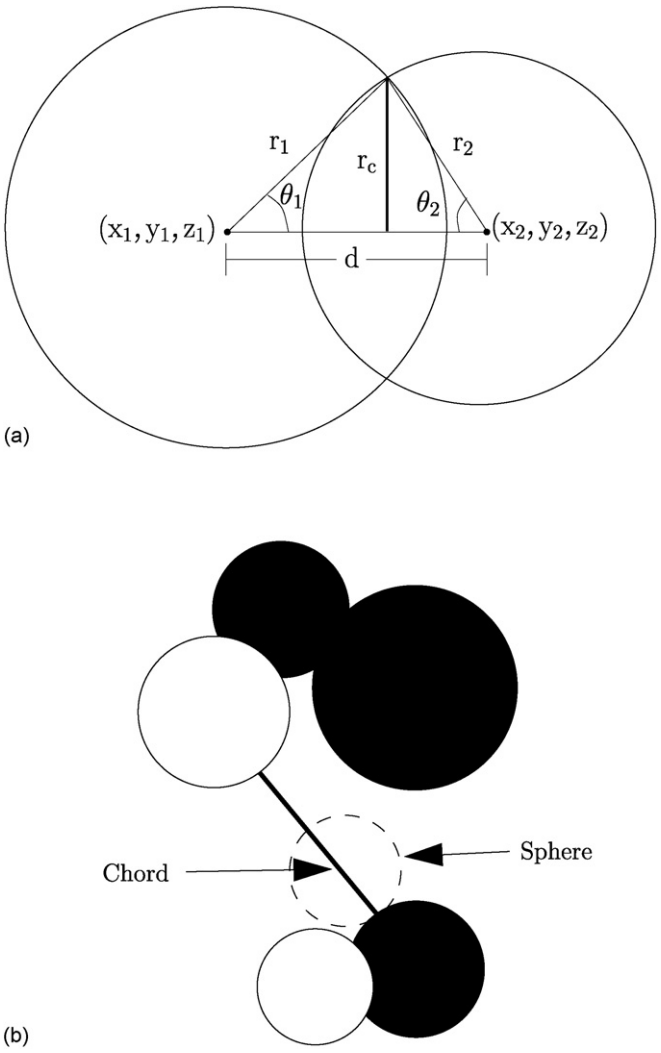

Fig. 1. Example of calculation of (a) TPBL using the analytical method and (b) pore size using the combined sphere growth/chord length method.

surface area of this triple overlap, we used the method described in Refs. [14,15].

$$d = \sqrt{(x_1 - x_2)^2 + (y_1 - y_2)^2 + (z_1 - z_2)^2} \quad (1)$$

$$\theta_1 = \cos^{-1}\left[\frac{r_1^2 + d^2 - r_2^2}{2r_1 d}\right] \quad (2)$$

$$\lambda_{\mathrm{TPBL}} = 2\pi r_1 \sin\theta_1 \quad (3)$$

These microstructural parameters were determined from an average of 20 structures. The standard deviation of the calculated parameter, based on the variance between these 20 structures, was found to depend on the percolation thresholds of the structure. For solid phase compositions within the bounds defined by the LSM and YSZ percolation (i.e. above the LSM and YSZ percolation thresholds), the standard deviation for both the active and total (ignoring percolation) TPBs was less than 2% of the mean. Outside the range of percolation bounds or close to the percolation threshold, the standard deviation for total TPBs remained below 2% of the mean however, for some calculations of the active TPBs outside the bounds of percolation threshold, the standard deviation was as high as 35% of the mean. For the internal surface area, the highest standard deviations were 18% of the mean but within the percolation bounds this would again fall to less than 2% of the mean. Additionaly, we averaged some parameters over 100 structures and found that the difference between an average of 20 structures and an average of 100 structures was less than 1% within the percolation limits and only as high as 5% at the percolation threshold.

The grid based technique applied a three-dimensional cartesian grid over the structure and counted the grid edges where two LSM and YSZ particles intersected with a pore. The active TPB was determined by counting only those particles which formed a percolating network. The analytical technique described above was preferred over the grid based technique due to the fact that the grid based technique approximated a sphere with a rectangular grid which always over predicted the edge length. However, unlike the grid counting technique, the analytical technique assumed that all pores belonged to a percolating network. As will be discussed later, the percentage of pores that belonged to a percolating network within the structures examined was found to be above 99% at a porosity above 25% and so we considered this assumption to be valid. All TPB, LSM–YSZ contact area and internal surface area values presented here were based on the analytical calculation.

2.3. Pore percolation

Pore percolation was determined using a grid based technique. This method assigned an integer to each percolating and non-percolating phase and swept through the structure to find the locations that satisfied the criterion for non-percolating pores. Due to grid approximation and the irregular geometry of the pore, this technique is thought to underestimate pore percolation since it was found that the grid based technique slightly underestimated the porosity compared to the analytical porosity. Nevertheless, a grid study determined that a grid size of around 20 nm gave an adequate balance between computation time and error between the analytical porosity and grid predicted porosity.

2.4. Pore size distribution

The pore size distribution was calculated based on a mixture of the chord length and the sphere growth method [16]. Chords are the line segments which can be drawn in the pore space between two solid particles and are one method used to represent the size of a pore. The sphere growth method grows a sphere inside a pore until it touches a solid particle. We used a mixture of these two methods to represent the pore size, as shown in Fig. 1(b). First, a sphere was grown inside a pore and then the chord length was measured starting at the point on the sphere where the sphere first contacted a solid particle. The chord was drawn through the centre of the sphere until it touched another solid particle. These calculations were done analytically by randomly picking a point within a pore which started the sphere growth. This method for calculating the pore size, unlike porosimetry or porometry techniques, gives the length scale that is used when calculating the Knudsen number. For each domain of size 15 μm × 15 μm × 15 μm, 1 million spheres were grown and 1 million chords were measured. To ensure independence of the pore size distribution from the number of chords, a comparison was made against the pore size distribution with 2 million chords for both high and low volume fractions of each structure set. In all cases, it was found that 1 million chords was sufficient. The chord lengths were binned into 10 nm groups to give the frequency of each pore size.

2.5. Domain size study

The domain size as well as the randomness of the generated structures influenced the results. For this reason, a study was performed to determine the minimum domain size as well as the minimum number of generated structures. With an average of 20 structures, it was found that increasing the domain size from

Table 1
Parameters for the "polydisperse" case.

Particle type	Mean	Standard deviation
LSM	$d_{LSM} = 0.73\,\mu m$	$\sigma_{LSM} = 0.3\,\mu m$
YSZ	$d_{YSZ} = 0.51\,\mu m$	$\sigma_{YSZ} = 0.3\,\mu m$

$15\,\mu m \times 15\,\mu m \times 15\,\mu m$ to $20\,\mu m \times 20\,\mu m \times 20\,\mu m$ changed the solution by less than 1% for the case with the largest particle sizes being considered in this work and for conditions above the LSM and YSZ percolation thresholds. For this reason, the calculations were performed on domain sizes of $15\,\mu m \times 15\,\mu m \times 15\,\mu m$ and averaged over 20 structures. Under these conditions, the number of particles within the domain varied depending on the particle size, but for mono-sized LSM and YSZ particles of 0.5 μm diameter and a structure porosity of 30%, the domain consisted of 38,300 particles.

3. Results and discussion

3.0.1. Sample structure

Fig. 2 shows a typical three-dimensional structure and its cross section. This structure has an overall porosity of 30%. The solid matrix has a composition of 56 vol% LSM and 46 vol% YSZ and the particle size distribution was chosen to represent the particle sizes of LSM (NexTech Materials, USA) and YSZ (Tosoh, USA) measured by the light scattering method. It should be noted that the particle size distribution of the LSM matched closely with a normal distribution. However, the YSZ powder size was bimodal and in this study was represented as a normal distribution using a best fit mean and standard deviation. The mean LSM and YSZ particle diameters were $d_{LSM} = 0.73\,\mu m$ and $d_{YSZ} = 0.51\,\mu m$ and the standard deviations were $\sigma_{LSM} = 0.3\,\mu m$ and $\sigma_{YSZ} = 0.3\,\mu m$. The structures generated here were meant to represent a typical electrode fabricated within our lab using an air spraying technique. Although an air spraying technique deposits many particles at once, for simplicity, we have assumed that the resting position of a particle is only affected by particles that have been previously deposited and not by the adjacent particles in the aerosol. This allows us to construct the structures one particle at a time. For the conditions at which the structure in Fig. 2 was built, most of the particles and pores were found to be percolating. Throughout this study, the set of LSM and YSZ particle sizes referred to as "polydisperse case" represent the NexTech LSM and Tosoh YSZ with the particle sizes described in Table 1.

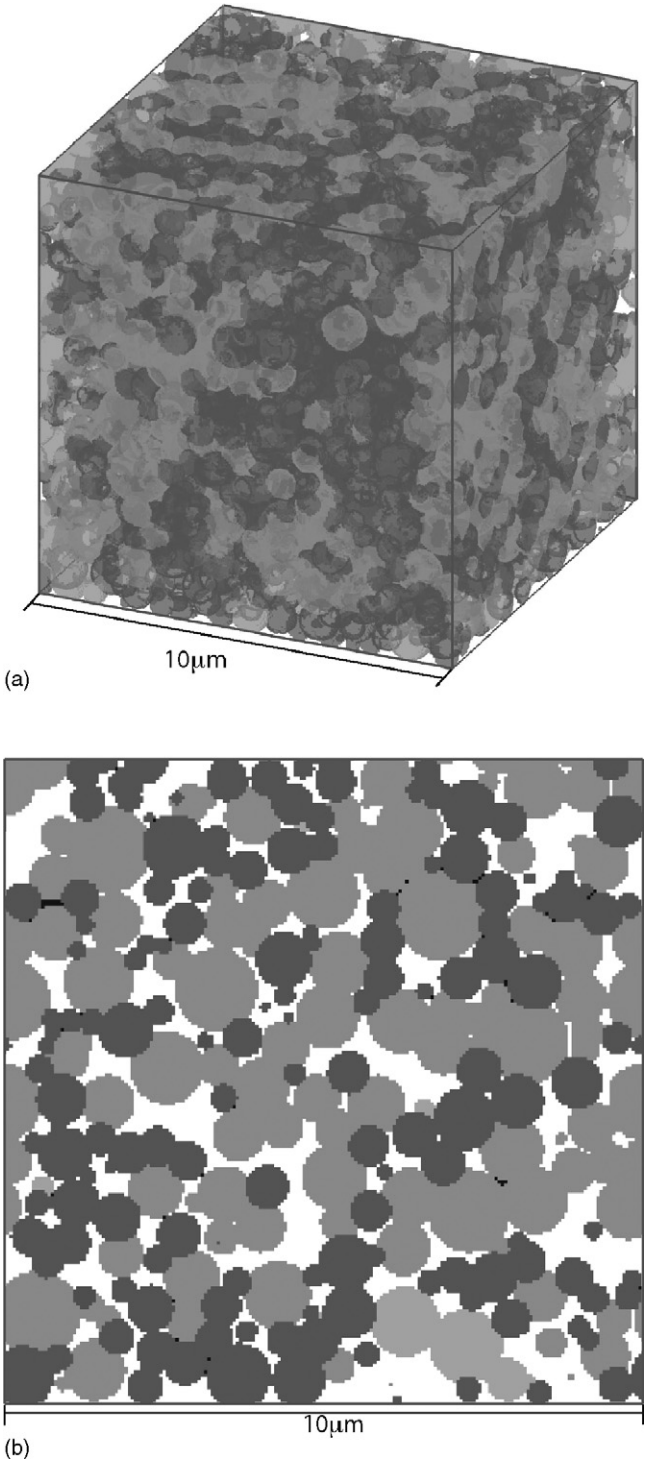

Fig. 2. Example of (a) 3D structure and (b) 2D cross-section with randomly distributed polydisperse LSM and YSZ particles. Light gray colored particles are LSM, dark gray colored particles are YSZ and black spots represent non-percolating pores. The structure is 54 vol% LSM with 30% porosity with $d_{LSM} = 0.73\,\mu m$, $d_{YSZ} = 0.51\,\mu m$, $\sigma_{LSM} = \sigma_{YSZ} = 0.3\,\mu m$. *Note*: This domain is smaller than the domain used for microstructural calculations.

3.1. Triple phase boundary length and contact area

3.1.1. Monosized particles

The total and active TPBL for 0.5 μm mono-sized particles is presented in Fig. 3. The drop in TPBL below 30 and above 70 vol% LSM is consistent with the small number of LSM particles percolating below 30 vol% and small number of YSZ particles percolating above 70 vol% LSM. For spherical particles of equal particle size, it is known that the percolation threshold occurs between 30 and 35 vol% (solids content) [17] and the maximum active TPBL lies between the percolation thresholds of LSM and YSZ.

Since the TPBL is increased when more LSM–YSZ particles come into contact, particle size and porosity are expected to influence the maximum TPBL value. Table 2 shows the TPBL at 30, 50 and 70 vol% LSM for various mono-sized particles and porosities. The trend shows that as particle size is reduced, TPBL increases and as porosity is reduced, TPBL also increases.

For mono-sized LSM and YSZ particles with different particle size ratios, the maximum TPBL shifts from 50 vol% LSM due to a shift in the percolation threshold of both LSM and YSZ. As shown in Fig. 4, when the mean LSM to YSZ particle size ratio (d_{LSM}/d_{YSZ}) increases, the maximum TPBL shifts towards higher LSM volume fractions and as this ratio decreases, the shift is to lower LSM volume fractions.

Interestingly, Fig. 4 shows that as the particle size ratio increases, the TPBL curves become less symmetric. One explanation for this is

Table 2
Active triple phase boundary length (TPBL) for various mono-sized particles and structure porosities.

Particle size (μm)	Porosity	TPBL at 50 vol% (μm μm^{-3})	TPBL at 60 vol% (μm μm^{-3})	TPBL at 70 vol% (μm μm^{-3})
$d_{LSM} = d_{YSZ} = 0.25$	30%	46.1 (±0.10%)	41.4 (±0.25%)	6.1 (±20%)
$d_{LSM} = d_{YSZ} = 0.5$	30%	11.6 (±0.44%)	10.4 (±0.92%)	2.3 (±35%)
$d_{LSM} = d_{YSZ} = 1.0$	30%	2.9 (±1.20%)	2.6 (±1.90%)	0.8 (±29%)
$d_{LSM} = d_{YSZ} = 0.5$	35%	8.2 (±0.44%)	6.8 (±1.01%)	1.2 (±21%)
$d_{LSM} = d_{YSZ} = 0.5$	40%	5.2 (±0.58%)	4.5 (±0.77%)	0.7 (±22%)

Note: Volume percents refer to LSM volume. Errors refer to standard deviation as a percentage of mean value.

that large particles can cast shadows which are regions not accessible to smaller particles. This phenomenon is shown in Fig. 5 which is a cross-sectional view of a structure generated with $d_{LSM} = 1.0\,\mu m$ and $d_{YSZ} = 0.25\,\mu m$. These shadows force smaller particles to agglomerate which causes less homogeneous mixing of the two particle types and can distort the particle percolation. In addition, pockets of large pores are formed around the locations where particle shadowing occurs. In reality, whether or not this behavior is observed would depend on the electrode fabrication technique. Processes that rely on thick pastes such as tape-casting or screen printing would likely observe less particle shadowing, however, in deposition processes such as wet powder spraying [18], particle shadowing may be more prevalent even with some particle rearrangement after solvent evaporation.

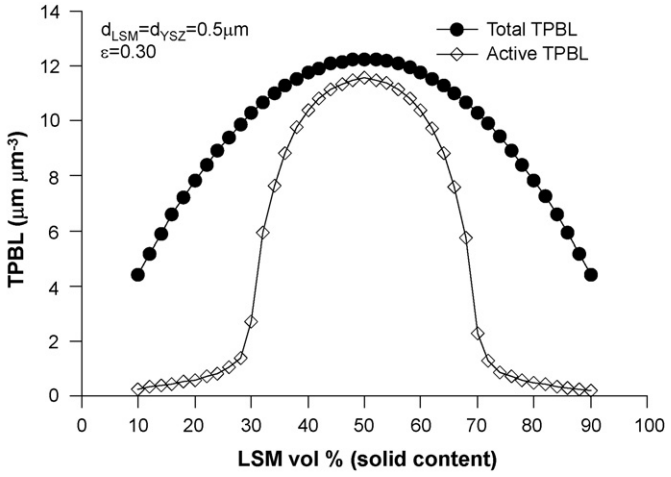

Fig. 3. Total and active TPB length as a function of solid volume fraction of LSM. Particle sizes were mono-sized LSM and YSZ with diameters of 0.5 μm and an electrode porosity of 30%.

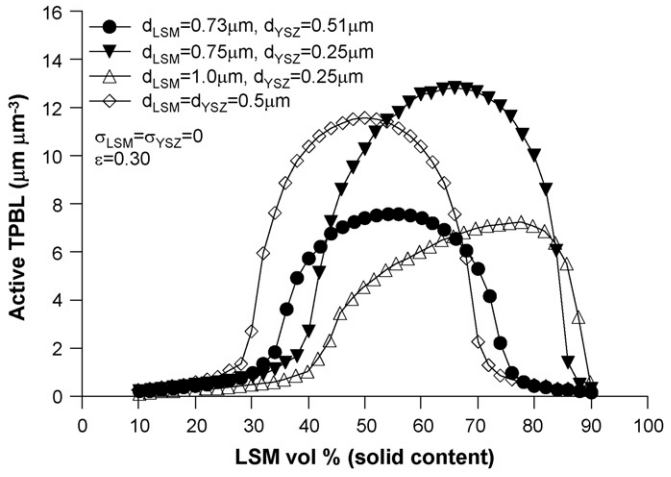

Fig. 4. Active TPBL for mono-sized LSM and YSZ particles with various d_{LSM}/d_{YSZ} particle size ratios and an electrode porosity of 30%.

3.1.2. Polydisperse particles

The discussion thus far has focused on mono-sized particles. However, ceramic powders are typically polydisperse powders, or, powders with a particle size distribution. A normal distribution to represent polydisperse powders with a specified mean and standard deviation has been used although any type of distribution can be applied. Fig. 6 shows how the particle size distribution (or the standard deviation of the particles) can affect the TPBL for mean LSM and YSZ particle sizes of 0.5 μm and over a range of particle size distributions.

As the particle size distribution increases (represented by an increase in the standard deviation of the particle size), the maximum TPBL decreases. The influence of particle size distribution on the active TPBL can be significant. As Fig. 6 shows, the TPBL of structures with a particle size distribution of $\sigma_{LSM} = \sigma_{YSZ} = 0.2\,\mu m$ is 35% lower than the TPBL of mono-sized particles ($\sigma_{LSM} = \sigma_{YSZ} = 0$) for the same mean particle diameters of $d_{LSM} = d_{YSZ} = 0.5\,\mu m$ at an LSM volume fraction of 0.5. Similarly, the TPBL for the polydisperse case was 40% smaller at an LSM volume fraction of 0.54 compared to the TPBL with the same mean particle size but $\sigma_{LSM} = \sigma_{YSZ} = 0\,\mu m$. There are two reasons for this decrease in TPBL: (1) the TPBL is influenced more strongly by the larger particles in the polydisperse powder than by the smaller particles; (2) the percentage of percolating particles decreases slightly with increasing particle size

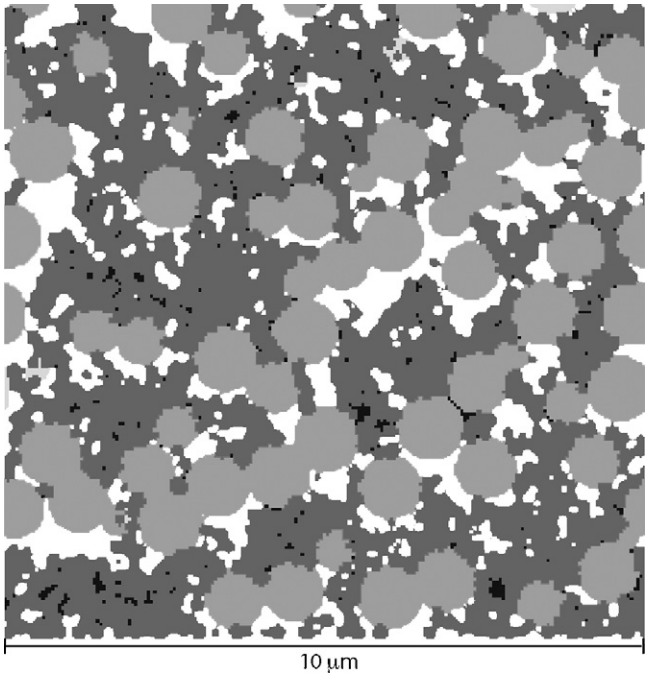

Fig. 5. Cross-sectional view of a structure showing particle shadowing with 30% electrode porosity and 50% LSM by volume. LSM particles (light gray), $d_{LSM} = 1.0\,\mu m$, block smaller YSZ particles (dark gray), $d_{YSZ} = 0.25\,\mu m$, forming areas of large pore sizes and non-uniform phase distribution. Non-percolating pores are shown in black.

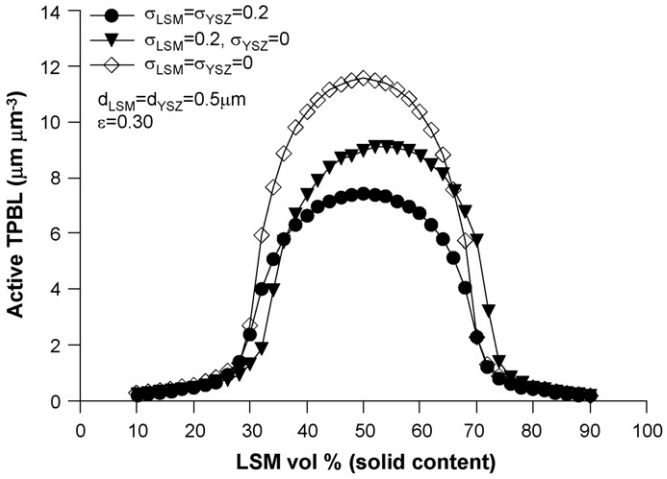

Fig. 6. Effect of LSM and YSZ particle size distributions on the active TPBL for constant mean particle size of 0.5 μm and constant electrode porosity of 30%.

distribution. Since the volume of a sphere is proportional to r^3, larger particles have a much larger volume than smaller particles. This means that a smaller number of total particles is required to fill the domain as the particle size distribution is increased and so the TPBL decreases because less LSM-YSZ particles come into contact. In addition, as the particle size distribution increases, the ratio between total TPBL and active TPBL is increased, meaning that a smaller proportion of particles are percolating when the particle size distribution of the powder is increased. Table 3 shows the percent difference between the total and active TPBL at 50 vol% LSM as well as the total number of particles in the domain for some cases presented in Fig. 6.

It is important to note that if the LSM and YSZ particle sizes are the same, even if they have particle size distributions, the LSM volume fraction that maximizes the TPBL will be 0.5. If the mean LSM and YSZ particles are the same but the standard deviations in the particle sizes are different, then this could shift the location of the maximum TPBL. Fig. 6 also shows the effect of having unequal LSM and YSZ particle size distributions. As the $\sigma_{YSZ}/\sigma_{LSM}$ ratio is increased while maintaining constant mean particle size, the location of maximum TPBL shifts from higher LSM volume fractions to lower LSM volume fractions and at the same time, for reasons given above, the maximum TPBL also decreases. The shift in the maximum TPBL is a consequence of shifting percolation thresholds. For the case presented in Fig. 6 of σ_{LSM}=0.2 μm and $\sigma_{YSZ} = 0$ μm the maximum TPBL occurs at 54 vol% LSM.

The above discussion can help to explain the TPBL profile for the polydisperse case which uses real particle size distributions (outlined in Table 1). Fig. 7(a) compares the active TPBL and Fig. 7(b) compares the active LSM–YSZ contact area for LSM and YSZ ceramic powders purchased from NexTech and Tosoh. From the TPBL curve and the above discussion, it is evident that the TPBL is decreased because the particle size distribution reduces the total number of particles in the control volume and the location of the maximum

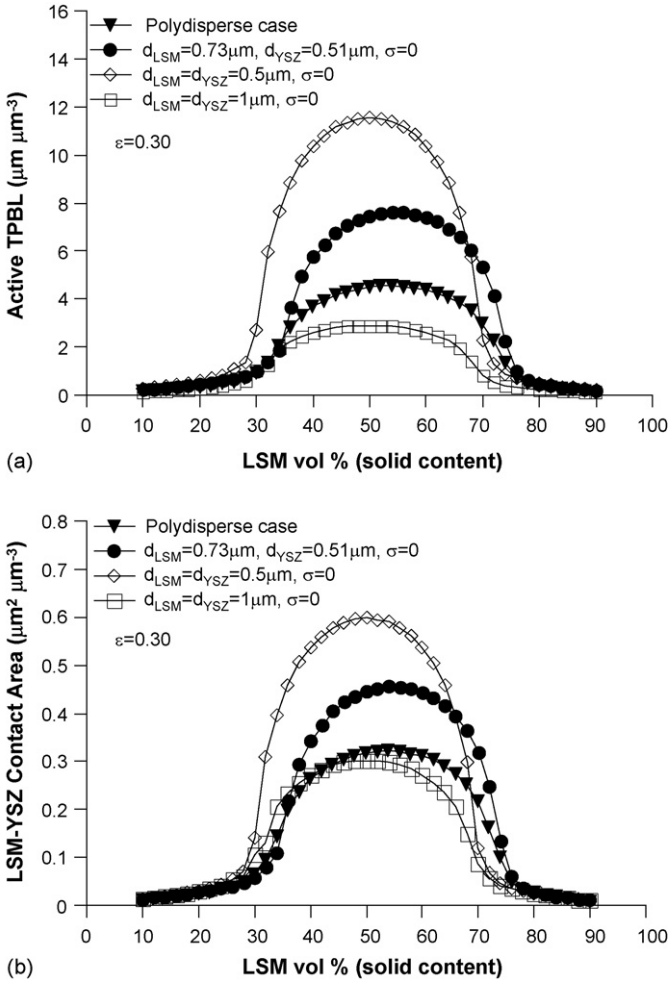

Fig. 7. Comparison of polydisperse case ($d_{LSM} = 0.73$ μm, $d_{YSZ} = 0.51$ μm, $\sigma_{LSM} = \sigma_{YSZ} = 0.3$ μm) against various other particle sizes with an electrode porosity of 30% for (a) active TPBL and (b) LSM–YSZ contact area for percolating particles.

TPBL is shifted slightly towards higher LSM vol% due to the differences in the mean LSM and YSZ particle sizes which influence the percolation threshold. The LSM volume that gives the maximum TPBL for this powder combination is 54 vol% LSM, resulting in a TPBL of 4.55 μm μm^{-3}. For comparison, a previous study using FIB-SEM on Ni/YSZ anodes [5] determined the TPBL to be 4.28 μm μm^{-3} for 32 vol% Ni (by solids) and 20% porosity, although the particle sizes were not mentioned. Also, a study using quantitative stereology [3] estimated TPBLs in the range of 1.5–2.0 μm μm^{-3} for Ni/YSZ anodes with 35% porosity, Ni and YSZ particle sizes between 1 and 2 μm and Ni vol% of roughly 50%.

The LSM–YSZ contact area shown in Fig. 7(b) can be helpful when considering mixed conductors or for electrochemical impedance spectroscopy analysis. For example, when calculating the double layer current during transient simulations such as impedance calculations, the double layer current can be calculated from $i_{dl} =$

Table 3
Percent difference between total and active TPBLs and number of total particles in the domain for some particle distributions in Fig. 6 and at 50 vol% LSM and a porosity of 30%.

Standard deviation in particle size (μm)	Percent difference from total and active TPBL	Total number of particles [a]	Percent of particles that are percolating
$\sigma_{LSM} = \sigma_{YSZ} = 0$	6.0%	38,300	98.2%
$\sigma_{LSM} = \sigma_{YSZ} = 0.05$	6.5%	37,200	97.9%
$\sigma_{LSM} = \sigma_{YSZ} = 0.1$	7.6%	34,210	97.2%
$\sigma_{LSM} = \sigma_{YSZ} = 0.2$	10.1%	26,760	94.8%

[a] Number of particles in 15 μm × 15 μm × 15 μm domain.

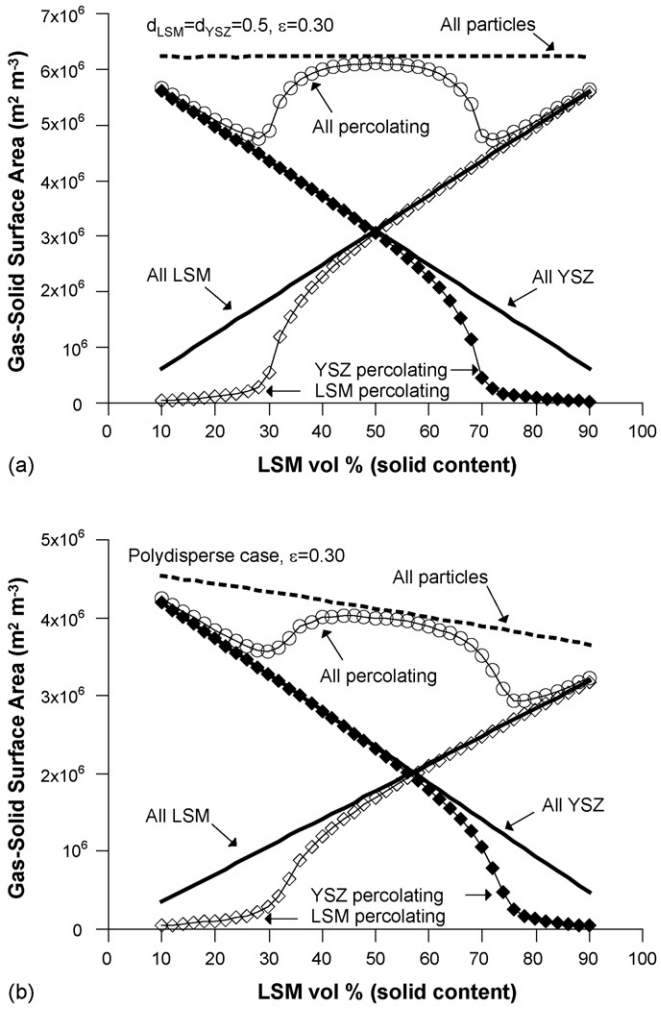

Fig. 8. Percolating and non-percolating gas–solid internal surface areas for LSM, YSZ and LSM + YSZ particles with an electrode porosity of 30% for (a) mono-sized particles ($d_{LSM} = d_{YSZ} = 0.5\ \mu m$) and (b) the polydisperse case.

$A_{dl}C_{dl}(d\eta/dt)$ [19,20] and requires knowledge of the active LSM–YSZ contact area presented in Fig. 7(b).

3.2. Gas–solid internal surface area

Since each phase within the electrode could have different adsorption characteristics, knowledge of the internal surface area for each phase is desirable. Fig. 8 shows the various internal surface areas calculated using a structure composed of mono-sized particles (Fig. 8(a)) as well as polydisperse particles (Fig. 8(b)).

As expected, the internal surface area of percolating particles increases quickly at the percolation threshold, which, for polydisperse particles, is different for LSM and YSZ. In the case of Fig. 8(b), the mean LSM particle size is larger than the mean YSZ particle size which, along with the particle size distribution, gives rise to the sloping total surface area (of percolating plus non-percolating particles) and the skewed curve for all percolating particles. For structures with a porosity of 30% and the polydisperse particle case, the total gas–solid surface area considering only percolating particles was $4 \times 10^6\ m^2\ m^{-3}$ for 50 vol% LSM and $3.6 \times 10^6\ m^2\ m^{-3}$ for 100 vol% LSM. For comparison, Ganeshananthan and Virkar [4] used quantitative stereolgy to estimate the same surface area for 100 vol% $La_{0.5}Sr_{0.5}CoO_{3-\delta}$ cathodes and found a value of $2.9 \times 10^6\ m^2\ m^{-3}$ while a FIB-SEM study [5] found a value of $4.6 \times 10^6\ m^2\ m^{-3}$ for Ni/YSZ anodes with 32 vol% Ni.

Particle size distribution as well as the electrode porosity can influence the internal surface area. Table 4 shows the influence of porosity on the internal surface area for the polydisperse case at LSM volume fractions of 0.5 and 0.7. Increasing the porosity of the structure reduces both the contact area of overlapping particles as well as the total number of contacts between each particle, thereby leaving a higher percentage of the surface of each particle exposed to the gas phase. Increasing the porosity also reduces the total number of particles within the domain though and the competition between increased surface area from less particle–particle contacts and reduced surface area from a smaller number of total particles manifests itself in only a slight increase of surface area as the porosity is increased.

3.3. Pore percolation and pore size

3.3.1. Pore percolation

A TPB is active when all three phases belong to percolating networks. There is little discussion in the literature on pore percolation, however, Abel et al. [21] considered the pore phase to be on the same footing as the metal and electrolyte phase for porous cermet anodes. By considering pores as spherical particles with percolation probabilities defined by the same relations as that for solid particles, the active TPB was underpredicted because as will be shown, unlike solid phase particles, nearly 100% of the pores percolate at 30% porosity. Accordingly, pore percolation is reported in this section.

Due to the irregular shape and size distribution of pores, predicting pore percolation is not as easy as using particle coordination theory nor can it be done by the analytical methods employed on the structures generated here. To investigate pore percolation, a grid was placed over each structure and the overall and effective porosity was counted. Fig. 9(a) shows the percentage of percolating pores as a function of porosity for two structures, one with mono-sized particles and one with particle size distributions. For each case, the percentage of percolating pores was greater than 99% for porosities greater than 25%. For comparison, Fig. 9(b) shows the percentage of percolating LSM particles for various LSM volume fractions. At 25% LSM vol%, less than 15% of LSM particles are percolating. This comparison outlines the differences that variable pore sizes and shapes can have on pore percolation compared to the solid particles. Also of note, polydisperse particles showed a larger fraction of percolating pores compared to mono-sized particles but the

Table 4
Gas–solid internal surface area ($m^2\ m^{-3}$) as a function of porosity at various LSM volume fractions for the polydisperse case.

Porosity	All percolating particles		Percolating LSM particles	
	50 vol% LSM	70 vol% LSM	50 vol% LSM	70 vol% LSM
30%	4.0×10^6 (±0.37%)	3.5×10^6 (±1.47%)	1.7×10^6 (±0.68%)	2.5×10^6 (±0.49%)
35%	4.1×10^6 (±0.35%)	3.6×10^6 (±1.88%)	1.7×10^6 (±0.75%)	2.6×10^6 (±0.49%)
40%	4.2×10^6 (±0.51%)	3.6×10^6 (±2.05%)	1.7×10^6 (±0.93%)	2.6×10^6 (±0.49%)

Note: Errors refer to the standard deviation as a percentage of mean value.

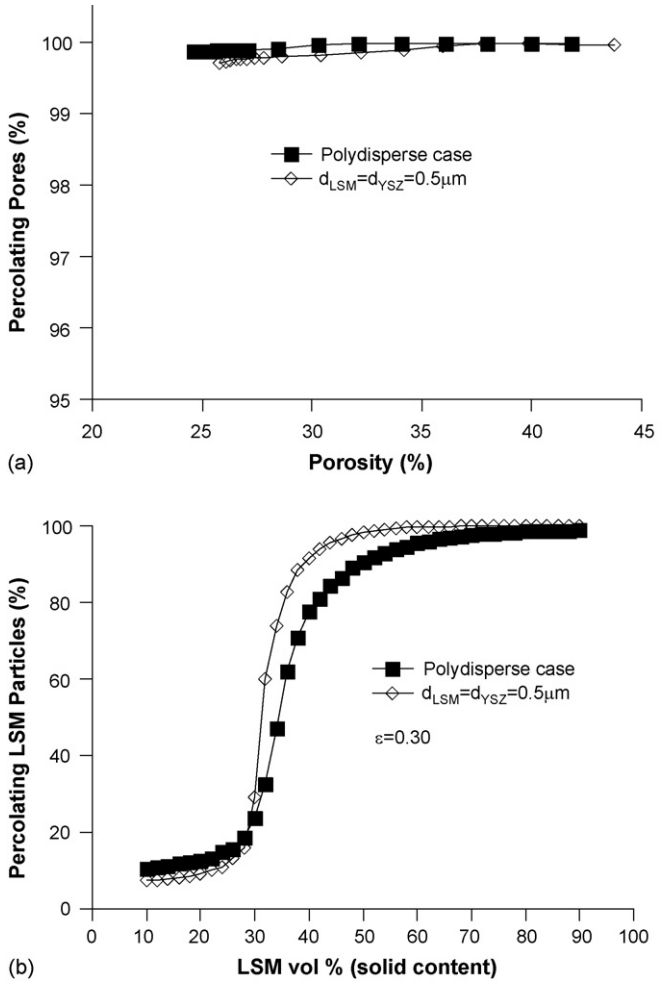

Fig. 9. (a) Percentage of percolating pores for electrode porosities between 25 and 45%, and (b) percentage of percolating LSM particles for and electrode porosity of 30%.

LSM particles in the polydisperse case showed a steep percolation threshold and ultimately, more LSM particles were percolating for the mono-sized particles compared to polydisperse particles.

3.3.2. Pore size

While the results above showed that for porosities typical of SOFC electrodes, more than 99% of pores were percolating, the pore structure can still influence the performance of the electrode through gas transport mechanisms. Therefore, although pore size characterization is difficult due to the irregular shape of the pores, some knowledge of the pore size is beneficial. Frequently it is assumed that the pore size is between 0.5 and 1 μm such as in Refs. [22,23], however, Cannarozzo et al. [24] calculated the pore size as a function of volume fraction and particle size. Using the technique by Cannarozzo et al. for an LSM particle diameter of 0.73 μm, YSZ particle diameter of 0.51 μm and an LSM volume fraction of 0.5 results in a pore size of 0.43 μm. These studies place gas transport in the transition regime for typical SOFC operating temperatures. This leads to the use of the Bosanquet equation for calculating the overall effective gas diffusivity from the effective binary gas diffusivity and the Knudsen diffusivity when modelling transport of gas through porous electrodes. Whether or not the transition regime approximation is valid depends on the Knudsen number defined by Eq. (4) which is calculated from the mean free path (MFP) of the gas molecule (Eq. (5)) and the characteristic length scale within the porous electrode,

$$Kn = \frac{\mathrm{MFP}}{d_{\mathrm{pore}}} \tag{4}$$

$$\mathrm{MFP} = \frac{RT}{\sqrt{2}\pi d_{\mathrm{gas}}^2 N_A P} \tag{5}$$

where d_{gas} is the diameter of the gas molecule, N_A is Avogadro's number, P is the gas pressure, and d_{pore} is the characteristic length. The characteristic length refers to the average distance that a molecule can travel before interacting with a solid surface, and can be taken to be the pore size. Knudsen numbers below 0.1 place gas transport in the continuum regime where the Knudsen diffusivity is not required, however, for Knudsen numbers roughly between 0.1 and 10, gas transport is in the transitional regime which requires the use of a Knudsen diffusion coefficient. For Knudsen numbers above 10, the free molecular flow regime dominates and using volume average techniques are difficult to justify. It is therefore important to have an accurate understanding of the pore size and how it is distributed throughout the electrode.

Fig. 10(a) compares the pore size distribution obtained on the polydisperse case for electrode porosities between 30–40% and 54 vol% LSM against structures generated with mono-sized particles, $d_{\mathrm{LSM}} = d_{\mathrm{YSZ}} = 0.5\ \mu\mathrm{m}$ (30% porosity, 50 vol% LSM). These pore size distributions were calculated using the combined sphere growth and chord length method outlined in Fig. 1(b). For the polydisperse case, a broad distribution of pore sizes was observed with less than

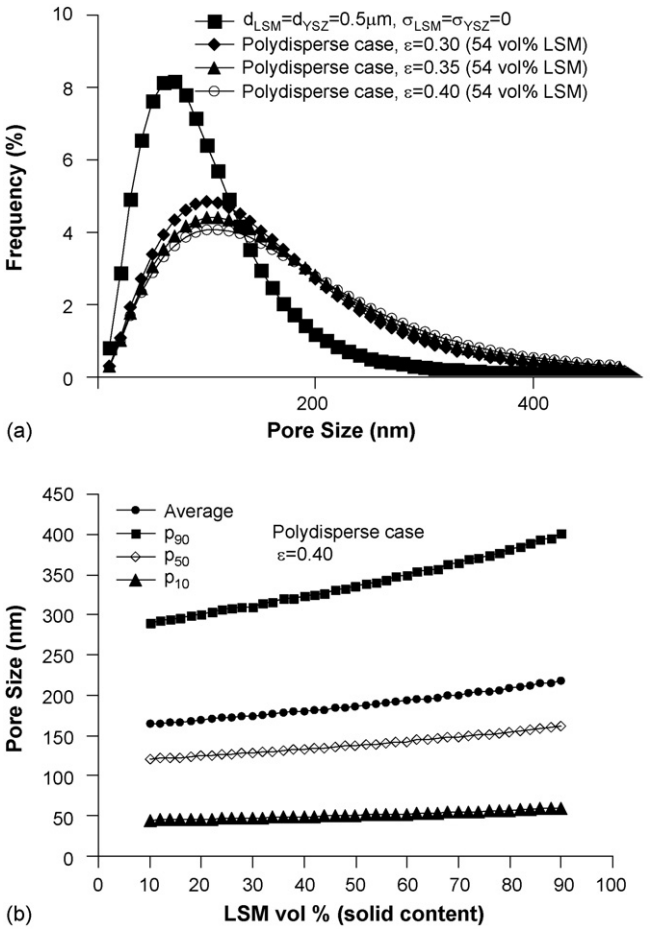

Fig. 10. (a) Pore size distribution for mono-sized particles with an electrode porosity of 30% and for the polydisperse case with an electrode porosity of 30, 35 and 40%. (b) Distribution of pore sizes for the polydisperse case with an electrode porosity of 30%. p_{90} means that 90% of all pores are smaller than this value.

Table 5
Mean free path and Knudsen numbers as a function of temperature and pore size.

Gas type	Temperature (°C)	Pore size (nm)	MFP (nm)	Knudsen number
O_2	850	190	372	2.0
O_2	850	140	372	2.7
O_2	850	50	372	7.5
O_2	750	190	340	1.8
H_2	850	190	598	3.1
H_2	850	140	598	4.3
H_2	850	50	598	11.9
H_2	750	190	545	2.9

2% of all pores being larger than 1 μm and the most frequent pore sizes were between 100 and 110 nm for porosities between 30 and 40%. For the mono-sized particles, just 0.5% of all pores were larger than 1 μm and the most frequent pore size was 70 nm.

In Fig. 10(b) we represent the pore size in a similar manner to how particle sizes are sometimes presented. For the polydisperse structure at 54 vol% LSM, 90% of the pores (p_{90}) were smaller than 350 nm, 50% of the pores (p_{50}) were smaller than 140 nm and 10% of the pores (p_{10}) were smaller than 50 nm with a number average pore size of 190 nm. Similar to the treatment by Cannarozzo et al., these pore sizes depend on the composition of the structure. As the LSM volume fraction increases, the pore sizes tend to increase since the LSM particles are larger than the YSZ particles. Although not shown here, for the mono-sized case, pore sizes remain constant throughout the entire range of LSM volume fraction. As mentioned above, it is frequently assumed that pore sizes are roughly 0.5 μm. This could be a result of a bias in SEM image analysis towards larger pore sizes since some SEM images do not have the resolution to view features much smaller than this. However, this does not necessarily conflict with the results obtained from our structure analysis. Fig. 10(b) shows that our p_{90} pore sizes are within the range commonly assumed, however, since our analysis is independent of the resolution of an image, we are able to estimate the full spectrum of pore sizes. In addition, we would predict larger pore sizes if our particle sizes were larger.

The results in Fig. 10 indicate that the average pore size may be quite a bit smaller than what is commonly assumed. It should also be mentioned that the length scale used in the calculation of the Knudsen number is precisely the length scale that is calculated here and shown in Fig. 10(b) and can differ significantly from results obtained through porosimetry. Table 5 shows some values of the Knudsen number calculated for the various pore sizes in Fig. 10(b). If we consider only the average pore size in the electrode, then the Knudsen number for both the anode and cathode falls within the transitional regime for temperatures between 750 and 850 °C. In fact, when considering only O_2, the Knudsen number in the cathode is less than 10 for typical operating conditions even when considering the smallest 10% of pores in the structure (p_{10}). However, Table 5 shows that for the H_2 molecule, when considering the smallest 10% of pores, it is possible to have Knudsen numbers above 10 due to the small size of the H_2 molecule. At the present time it is unknown how the transport of gas is influenced by distributed pore structures such as those observed in Fig. 10(b) which could result in flow regimes falling within both the transitional regime and the free molecular flow regime, especially for the SOFC anode.

4. Conclusion

A method of generating three-dimensional composite SOFC electrode structures of randomly distributed particles, with particle size distributions, has been presented. With these structures, important microstructural information can be obtained, most notably, the triple phase boundary length and LSM–YSZ contact area, internal surface area, percolation of particles and pores as well as pore size distributions. For mono-sized particles, trends in the particle percolation, and hence the triple phase boundary length, compared well with coordination number theory. The triple phase boundary length was maximized for small particles with narrow distributions. Larger particle size distributions reduced the triple phase boundary length. The results also indicated that over 99% of pores belonged to a percolating network at porosities larger than 25%. Also, for structures created using real particle size distributions and typical compositions, 90% of the pore sizes were found to be smaller than 350 nm, which implies that O_2 and H_2 gas transport is in the transitional regime at temperatures between 750 and 850 °C. The average pore size was 2.5 times smaller than what is commonly assumed in the literature. Additionally, under certain circumstances, a small fraction of the pores were found to be small enough to place gas transport in the anode in the free molecular flow regime.

Acknowledgements

This research was supported through the AUTO21 Network of Centres of Excellence and through funding to the NSERC Solid Oxide Fuel Cell Canada Strategic Research Network from the Natural Science and Engineering Research Council (NSERC) and other sponsors listed at www.sofccanada.com.

References

[1] B. Kenney, K. Karan, J. Electrochem. Soc. 153 (6) (2006) A1172–A1180.
[2] M. Ostergard, C. Clausen, C. Bagger, M. Mogensen, Electrochim. Acta 40 (12) (1995) 1971–1981.
[3] Y. Sakamoto, N. Shikazono, N. Kasagi, Effects of electrode microstructure on polarization characteristics of SOFC anodes, in: Sixth International Fuel Cell Science, Engineering and Technology Conference, June 16–18, 2008.
[4] R. Ganeshananthan, A. Virkar, Measurement of transport properties of perovskite cathodes, in: Solid Oxide Fuel Cells IX (SOFC-IX), vol. 2, The Electrochemical Society, 2005, pp. 1487–1498.
[5] J.R. Wilson, W. Kobsiriphat, R. Mendoza, H.-Y. Chen, J.M. Hiller, D.J. Miller, K. Thornton, P.W. Voorhees, S.B. Adler, S.A. Barnett, Nature 5 (2006) 541–544.
[6] P. Costamagna, P. Costa, V. Antonucci, Electrochim. Acta 43 (3–4) (1998) 375–394.
[7] S. Sunde, J. Electroceram. 5 (2) (2000) 153–182.
[8] S.H. Chan, X.J. Chen, K.A. Khor, J. Electrochem. Soc. 151 (1) (2004) A164–A172.
[9] B. Kenney, K. Karan, Solid State Ionics 178 (2007) 297–306.
[10] L. Schneider, C. Martin, Y. Bultel, L. Dessemond, D. Bouvard, Electrochim. Acta 52 (9) (2007) 3190–3198.
[11] J. Golbert, C.S. Adjiman, N.P. Brandon, Ind. Eng. Chem. Res. 47 (2008) 7693–7699.
[12] A.S. Martinez, J. Brouwer, Electrochim. Acta 53 (2008) 3597–3609.
[13] A. Ali, X. Wen, K. Nandakumar, J. Luo, K.T. Chuang, J. Power Sources 185 (2) (2008) 961–966.
[14] K.D. Gibson, H.A. Scheraga, J. Phys. Chem. 91 (1987) 4121–4122.
[15] K.D. Gibson, H.A. Scherag, Mol. Phys. 64 (4) (1988) 641–644.
[16] S. Torquato, Random Heterogeneous Materials: Microstructure and Macroscopic Properties, vol. 16, Springer, 2002.
[17] D. Bouvard, F. Lange, Acta Metall. Mater. 39 (12) (1991) 3083–3090.
[18] N. Oishi, Y. Yoo, I. Davidson, J. Am. Ceram. Soc. 90 (5) (2007) 1365–1369.
[19] W.G. Bessler, S. Gewies, M. Vogler, Electrochim. Acta 53 (2007) 1782–1800.
[20] J.I. Gazzarri, O. Kesler, J. Power Sources 167 (2007) 100–110.
[21] J. Abel, A.A. Kornyshev, W. Lehnert, J. Electrochem. Soc. 144 (12) (1997) 4253–4259.
[22] H. Zhu, R. Kee, V. Janardhanan, O. Deutschmann, D. Goodwin, J. Electrochem. Soc. 152 (12) (2005) A2427–A2440.
[23] R. Suwanwarangkul, E. Croiset, M.W. Fowler, P.L. Douglas, E. Entchev, M.A. Douglas, J. Power Sources 122 (2003) 9–18.
[24] M. Cannarozzo, A. Del Borghi, P. Costamagna, J. Appl. Electrochem. 38 (2008) 1011–1018.